This is a preprint, the final version is subject to change, of the American Mineralogist (MSA)
Cite as Authors (Year) Title. American Mineralogist, in press.
DOI: https://doi.org/10.2138/am-2020-6984

Plagcheck: no concerns
Tables?: 3 small
Word Count: ~9,100
Prod notes: make sure tables in file before RE

Swelling capacity of mixed talc-like/stevensite layers in white/green clay infillings ('deweylite'/'garnierite') from serpentine veins of faulted peridotites, New Caledonia

REVISION 2

Lionel FONTENEAU [1], Laurent CANER [2*], Sabine PETIT [2], Farid JUILLOT [3], Florian PLOQUIN [3], Emmanuel FRITSCH [3]

[1]Corescan Pty Ltd, 1/127 Grandstand Road, 6104 Ascot, WA, Australia

[2] Université de Poitiers, Institut de Chimie des Milieux et Matériaux de Poitiers, IC2MP UMR 7285 CNRS, *5 rue Albert Turpain, TSA51106*, 86073 Poitiers cedex 9, France

* Corresponding author, e-mail: laurent.caner@univ-poitiers.fr

[3] Institut de Minéralogie, de Physique des Matériaux et de Cosmochimie (IMPMC), Sorbonne Universités – Université Pierre et Marie Curie UPMC, UMR CNRS 7590, Museum National d'Histoire Naturelle, UMR IRD 206, 101 Promenade Roger Laroque, Anse Vata, 98848, Nouméa, New Caledonia

Abstract: White (Mg-rich) and green (Ni-rich) clay infillings ('deweylite'/'garnierite') found in serpentine veins of faulted peridotite formations from New Caledonia consist of an intimate mixture of fine-grained and poorly ordered 1:1 and 2:1 layer silicates, commonly referred to as non-expandable serpentine-like (SL) and talc-like (TL) minerals. New data on the swelling and shrinking capacity of these layer silicates were gathered from X-ray diffraction (XRD)

This is a preprint, the final version is subject to change, of the American Mineralogist (MSA)
Cite as Authors (Year) Title. American Mineralogist, in press.
DOI: https://doi.org/10.2138/am-2020-6984

after saturation of the clay fractions with different cations (Ca^{2+}, Li^{+}, K^{+}), ethylene glycol (EG) solvation, and heat treatments. Simultaneously, layer charge distribution and vacancy density, respectively, were investigated by FTIR spectroscopy on NH_4-saturated clay fractions and XRD on Li-saturated clay fractions before and after heating (Hofmann Klemen treatment). Five clay infillings, with dominant 2:1 layer silicates and variable Ni contents, were selected for this study, from a large set of veinlets, according to their swelling capacity. The crystal chemistry of these samples was characterized by FTIR spectroscopy and bulk chemical analyses.

The swelling ability of the clay infillings is attributed to the 2:1 layer silicates. It does not seem to be affected by the relative fraction of Mg and Ni in their octahedral sheets. In XRD patterns, the swelling ability is reflected by slight shifts of the basal reflection of the 2:1 layer silicates towards low angles for bulk samples and by splitting of the peak into two contributions for clay fractions saturated with Ca (or Li) and solvated with EG. The split increases with the swelling capacity of the sample. It originates mainly from octahedral-layer charge generated by vacant sites. Such results lead us to consider the 2:1 layer silicates of the infillings as an intimate mixture of non-expandable (TL) and expandable (stevensite) phases. In agreement with previous studies which suggested a contribution of hydrothermal processes in the alteration of serpentine species into 2:1 layer silicates, we propose that the proportion of expandable phases in the clay infillings (or vacancy sites in the octahedral sheets of the 2:1 layer silicates) could be used as an efficient means for assessing the temperature of their formation. Clay infillings mostly made of stevensite would have formed at ambient temperatures, whereas those consisting mainly of non-expandable TL would have formed at higher temperatures.

This is a preprint, the final version is subject to change, of the American Mineralogist (MSA)
Cite as Authors (Year) Title. American Mineralogist, in press.
DOI: https://doi.org/10.2138/am-2020-6984

Introduction

Nickeliferous laterites developed on ultramafic rocks (e.g. dunite, harzburgite) in tropical regions are of particular interest as they commonly contain two kinds of Ni-silicate ores: (1) 'clay silicate' ores, and (2) 'hydrous Mg/Ni silicate' ores (Brand et al., 1998; Gleeson et al., 2004; Freyssinet et al., 2005; Wells et al., 2009, Fritsch et al. 2016). Layer silicates of the 'clay silicate' ores are mostly composed of swelling dioctahedral 2:1 layer silicates (smectite) such as Fe-nontronite, Fe-montmorillonite, and Al-beidellite (e.g. Gaudin et al., 2004). They usually occur in saprolite, at the bottom of thick and poorly drained lateritic profiles developed on ultramafic rocks and correspond to low-grade Ni-deposits (less than 4 wt % Ni). By contrast, layer silicates of the 'hydrous Mg/Ni silicate' ores mostly consist of weakly expandable trioctahedral 1:1 and 2:1 layer silicates of the serpentine (structural formula: $Si_2[Mg,Ni]_3O_5(OH)_4$) and talc (structural formula: $Si_4[Mg,Ni]_3O_{10}(OH)_2$) mineral groups (e.g. Brindley and Hang, 1973; Brindley and Wan, 1979, Brindley, 1980; Manceau and Calas, 1985; Tauler et al., 2009; Wells et al., 2009). Because of their small size and low crystal order (stacking defects and vacancies), these layer silicates are commonly referred to as serpentine-like (SL) and talc-like (TL) minerals (Villanova-de-Benavent et al., 2014; 2019; Fritsch et al., 2016). Because of their same ionic charge (+2) and similar ionic radii, Ni (0.69 Å) can replace Mg (0.72 Å) in the octahedral sites of trioctahedral clay minerals leading to various mineral series with large ranges in chemical composition (Faust, 1966, Faust and Murata, 1953, Brindley et al., 1977). Mineral associations of trioctahedral 1:1 and 2:1 clay minerals in veinlets are termed deweylite for the white Mg-rich phases (Bish and Brindley, 1978) and garnierite for the bluish green Ni-rich phases (Pecora et al., 1949). Kerolite is the magnesium-rich end-member, while pimelite is the nickeliferous end-member for the TL mineral series. Such layer silicates are present at depth in white (deweylite) to green (garnierite) clay infillings of faulted saprock and observed in both freely and poorly drained lateritic profiles

(Cluzel, 2006; Cluzel and Vigier 2008; Fritsch et al., 2016; 2019; Villanova-de-Benavent et al., 2014). They are widely observed in peridotite massifs of New Caledonia and are related to high-grade Ni-deposits (up to 32 wt % Ni).

The two kinds of silicate ores are therefore associated with contrasting geochemical and structural environments, which suggest that they might have formed under distinct weathering (or alteration) conditions. Whereas the 'clay silicate' ores are commonly associated with the vertical development of thick lateritic profiles under poorly drained conditions (e.g. Gaudin et al., 2004), recent studies in New Caledonia suggest that the 'hydrous Mg/Ni layer silicate' ores might have formed in reactivated faults from the hydrothermal alteration of serpentine species into TL minerals during the dismantling and cooling of the ophiolite nappe (Fritsch et al., 2016; 2019; Cathelineau et al., 2017). Hydrous Mg/Ni layer silicates were described elsewhere in different climatic environments but in similar geological settings, for example in serpentinite at structural contacts in Greece (Christidis and Mitsis, 2006) and in Italy (Capitani and Ventruti, 2018).

Detailed textural and mineralogical investigations on the serpentinised and mineralised faults show that minerals of the serpentine group are predominant at the margin of the veins, whereas those of the talc group prevail in association with quartz in their central part (Christidis and Mitsis, 2006; Fritsch et al., 2016, 2019). In addition, TL minerals have locally been described in association with stevensite (Brindley and Hang, 1973, Wiéwióra et al., 1982) or as mixed layers stevensite-talc (Eberl et al., 1982; Christidis and Mitsis, 2006). Stevensite is considered a swelling trioctahedral (Mg, Ni) 2:1 layer silicate (smectite) with a chemical composition similar to that reported for TL minerals but with vacant sites in its octahedral sheets (Christidis and Mitsis, 2006). Scarcely reported worldwide, this swelling phase has most likely been overlooked in recent mineralogical studies on Ni-laterite deposits

(Villanova-de-Benavent et al., 2014; 2016; 2019; Fritsch et al., 2016; 2019; Cathelineau et al., 2016; Capitani and Ventruti, 2017; Tauler et al., 2017; Munoz et al., 2019).

This paper describes, for the first time, the occurrence of stevensite in vein-infillings of reactivated faults from peridotitic formations of New Caledonia. Five samples of white (deweylite) and bluish green (garnierite) clay infillings, with distinct swelling abilities, were selected from a large set of vein infillings to investigate the relationship between swelling capacity, crystal chemistry, charge deficiency, and structural disorder (stacking defects and vacancies). Our results aim at deciphering the mechanisms involved in these changes of swelling and crystallographic properties with the ultimate goal of identifying the conditions of formation of the hydrous Mg/Ni layer silicates.

Materials and Methods

The five samples investigated in this study (Figures 1 and 2) belong to a large set of clay infillings, whose texture, mineralogy and chemistry have been determined by Fritsch et al. (2016, 2019). They were collected at depth in the saprock, more specifically, in fractures of highly serpentinised zones of two peridotite formations (mainly harzburgite) of the New Caledonian mainland (Figure 1): (i) the Koniambo klippe (mining site "Manguen") on the Western coast (MG1aWill, MG3aWill) and (ii) the Poro klippe (mining site "La Française" of the CFTMC) on the Eastern coast (BONBR2a, BONBR2c, LFSTA5a2). Both klippes are known for an abundance of fractures and associated crosscutting mineralised veins (also named box-works or "Minerai quadrillé" in the French literature), which grade from white (deweylite) to bluish green (garnierite) according to the relative proportion of Mg and Ni. The five samples belong to an ultimate episode of clay infillings predominantly made of 2:1 layer silicates (see Fritsch et al. 2016 for a more detailed description of the vein-infillings). They

were selected according to their ability to swell and shrink. Shrinking in the field leads to the development of cracks along the clay infillings after exposure of the mining cuts to air (Figure 2b). In thin sections it is related to the occurrence of a dense network of cracks, more specifically in Ni-rich bands of the infillings (Figure 2d).

Samples were air-dried and crushed with a pestle and mortar before chemical and mineralogical investigations. Chemical analyses of the samples were carried out by digestion of 1000 mg of the finely powdered sample in a high-pressure TFM Teflon vessel using an ETHOS 1600 MILESTONE microwave system, with samples digested using a mixture of 3mL of HCl (37%), 2mL of HNO_3 (65%), 1.5mL of HF (40%) and 5mL of H_3BO_3 (5%). After digestion the solution was diluted with osmosed water. Si, Mg, Ni, Co, Al, Fe, Ca, Cr and Cu concentrations were determined using a Perkin Elmer 1100b atomic absorption spectrophotometer. Loss on ignition (LOI) was determined after heating at 1000 ºC.

To determine the clay (<2 μm fraction) mineralogy, bulk samples were gently ground in agate mortar and sieved at 50 μm. The < 50μm fractions were dispersed into 1 mol L^{-1} NaCl aided by ultrasonication. This procedure was reproduced five times to ensure complete Na saturation and dispersion of the samples. The clay fractions were then obtained by centrifugation according to the Stokes'law. The suspended clay fractions were flocculated with 0.5 mol. L^{-1} $CaCl_2$ and divided into aliquots for saturation with different cations (Ca^{2+}, K^+, Li^+ and NH_4^+). The aliquots were treated five times with 0.5 mol. L^{-1} $CaCl_2$, and 1 mol. L^{-1} KCl, LiCl, and NH_4Cl, and washed with osmosed water to remove excess salts until a negative test with 1 M $AgNO_3$ was obtained. As Li^+ and NH_4^+ may enhance dispersion and formation of gels, the Li- and NH_4-saturated samples were washed in ethanol instead of osmosed water and ultra-centrifuged (30000 g). K-saturated samples were heated at 20, 150, 350 and 550°C and examined by XRD. Ca-saturated and Li-saturated samples were analysed by XRD both in an air-dried (AD) state and after ethylene glycol solvation (EG vapour at 50

ºC overnight) to assess the swelling capacity of the layer silicates. The Hofmann-Klemen (HK) treatment (Hofmann and Klemen, 1950; Greene Kelly, 1953, 1955) was also applied to the five clay samples to reveal the possible occurrence of octahedral vacancies in clay minerals. The Li-saturated samples were heated overnight at 300 °C to induce migration of Li^+ into octahedral vacancies of the phyllosilicates. For trioctahedral smectites the swelling behaviour of the layers after HK treatment depends on the location of the charge. When the charge originates from the octahedral sheet, the Li saturation and heating result in only partial neutralisation of the charge by migration of a monovalent cation (Li^+) in the octahedral vacancy, and the layers may remain expandable in EG (Petit et al., 2008, Gaudin et al., 2004) or glycerol (Brindley and Brown, 1980). Oriented clay mounts were obtained by dropping a small amount of clay suspensions onto glass slides (or zero background Si wafers) and drying them at room temperature. For some preparations the suspensions were made in ethanol to avoid the formation of gels.

Bulk mineralogy of samples was determined by XRD on randomly oriented powders in the step scan mode in the range 2–65° 2θ with steps of 0.025° 2θ and a counting time of 229 s per step using a Bruker D8 Advance diffractometer (Cu Kα radiation, 40 kV and 40 mA) equipped with a Lynx eye detector. XRD patterns of oriented samples were recorded in both AD and EG solvated states in the step scan mode in the range 2–35° 2θ with steps of 0.016° 2θ and a counting time of 229 s. Background stripping was carried out on XRD patterns of oriented preparations, and the *00l* diffraction peaks of the layer silicates were decomposed into Gaussian curves with Fityk® (Wojdyr, 2010) to determine peak positions, peak areas, and full width at half maximum (FWHM), the latter being converted into coherent scattering domain sizes (CSDS) in the c direction (defined by the statistical range of number of layers: N).

Fourier transform infrared (FTIR) spectra of bulk and <2μm samples were recorded in the middle IR 400-4000 cm^{-1} range (MIR) using a Nicolet 760 FTIR spectrometer in transmission mode with a 4 cm^{-1} resolution. The spectrometer was continuously purged with dry, CO_2-depleted air. MIR spectra were recorded from disks prepared by mixing 1 mg of the sample with 150 mg of KBr and pressing them at 10 $tons.cm^{-2}$. Pellets were heated overnight at 110 °C to remove absorbed water before the FTIR spectra were recorded. Layer charge distribution, (i.e. tetrahedral (Te), octahedral (Oc) and variable charges), was estimated by quantifying the amount of NH_4^+ fixed by the samples, before and after Li-saturation and heating at 300 °C, using the integrated intensity of the υ_4NH_4 band at 1400 cm^{-1} of normalised FTIR spectra (Petit et al., 1998, 2002, 2008; Gaudin et al., 2004, Mano et al., 2014). The NH_4^+ fixed by the swelling layers of the raw samples corresponds to the total charge of the layers (permanent [Te + Oc] + variable edge charges). It is considered as the CEC at the pH of the NH_4Cl solution. After Li saturation and heating at 300 °C (HK test), the amount of NH_4^+ fixed by the layer silicates corresponded to the remaining charge, not neutralised by migration of Li^+ in the octahedral sites (Petit et al., 1998, 2006). FTIR spectra of the NH_4^+-saturated samples (NH_4^+ and $Li_{300}NH_4^+$) were recorded using the same amount of clay and normalised to the OH vibration bands of the main SiO band around 1020 cm^{-1}.

Near infrared (NIR) spectra were recorded at a resolution of 4 cm^{-1} from 4000 to 10,000 cm^{-1} in a glass vial, with a Thermo Scientific Integrating Sphere (diffuse reflectance) with an internal InGaAs detector coupled to a Thermo Scientific Nicolet 6700 FT-IR spectrometer.

RESULTS

Mineralogy and crystal chemistry

This is a preprint, the final version is subject to change, of the American Mineralogist (MSA)
Cite as Authors (Year) Title. American Mineralogist, in press.
DOI: https://doi.org/10.2138/am-2020-6984

Mineralogical and crystal chemical characteristics of hydrous Mg/Ni layer silicates from the five samples were determined using XRD (Figures 3, 6 and 9), FTIR spectroscopy (Figure 4, Table 2), and bulk chemical analyses (Table 1, Figure 5). XRD patterns and FTIR spectra are stacked in the figures according to the ability of the samples to swell (the less expandable at the bottom and the more expandable at the top).

Bulk mineralogy

In agreement with previous studies carried out on a larger set of mineralised veins (Fritsch et al. 2016), powder XRD patterns of bulk samples (Figure 3) show that the clay infillings of the samples consist of a mixture of 7 Å-type (1:1) layer silicates of the serpentine mineral group (peaks at 7.32 to 7.38 Å and 3.64 to 3.66 Å) and 10 Å-type (2:1) layer silicates of the talc mineral group (peaks at 10.01 to 11.12 Å and at 3.20 to 3.22 Å). The powder XRD pattern of the less expandable sample (MG1aWill) also displays quartz (Qz). According to XRD results, sample BONBR2c, which is free of Ni (white color), is the richest in SL components and contains TL minerals with poorly resolved *001* reflection. Conversely, powder XRD patterns of samples with greater Ni contents (bluish green colours) present better resolved *001* reflection for TL minerals and smaller proportions of serpentine. The peak at ~ 1.525 Å for the shared 06-33 reflection of 1:1 and 2:1 layer silicates indicates that all samples consist of pure tri-octahedral clay minerals with a dominance of bivalent cations (Mg^{2+} and Ni^{2+}) in the octahedral sheets (Table 1, Figure 3).

The broad basal *001* reflections and the presence of two-dimensional hk bands (20-13) attest to small coherent scattering domain sizes (CSDS), and structural disorder (stacking defects and vacancies) that enable to refer the layer silicates to serpentine-like (SL) and talc-like (TL) minerals (Brindley and Hang, 1973; Brindley et al., 1977; Bish and Brindley, 1978; Brindley and Brown, 1980; Decarreau et al., 1987; Proenza et al. 2008; Tauler et al., 2009; Villanova-

de-Benavent et al., 2014; Fritsch et al. 2016). In the XRD patterns of the less expandable (MG1aWill) and the most expandable (BONBR2c) samples, the sharp reflection at ~ 2.51 Å (and to a lesser extent that at ~ 2.45 Å) is superimposed to the broad 20-13 band (Figure 3). These sharp reflections, which overlap with broader reflections of cryptocrystalline SL and TL, suggest additional occurrence of crystalline serpentine (Srp) as reported by Fritsch et al. (2016) based on XRD patterns (reflection at 2.51 Å for lizardite 1T and 2.45 Å for chrysotile 2M) and HRTEM images (large platelets of lizardite and tubular shaped chrysotile). These variations are also consistent with the presence of a peak asymmetry on the low-angle side of the basal reflections. For the most expandable sample (BONBR2c), the first basal reflection of the 7 Å layer silicates was fitted with two Gaussians (not shown): (i) the first one with a narrow reflection at 7.32 Å (CSDS: 60-75 *N*) which is attributed to well-crystallised serpentine residues (Srp) and (ii) the second wide one at 7.38 Å with smaller CSDS (15 *N*) corresponding to poorly ordered SL species (Fritsch et al., 2016). The statistical range of the number of layers (N) can vary widely for the 1:1 layer silicates (from 75 to 15), according to the amount of serpentine residues (Srp) in the samples. By contrast, the CSDS value is systematically smaller for the 10 Å-type layer silicates ($8 < N < 18$), thereby underlining the small size of the poorly crystallized TL minerals.

Mg and Ni speciation in the layer silicates

FTIR spectra (Figure 4) confirm the mineral composition of the samples (mostly made of TL and SL minerals) and reveal the distribution of divalent cations (Mg and Ni) in the octahedral sites of the layer silicates (Farmer, 1974; Gerard and Herbillon, 1983; Balan et al., 2002; Petit, 2005; Christidis and Mitsis, 2006; Jagannadha Reddy et al., 2009; Mano et al., 2014; Baron and Petit, 2016; Baron et al., 2016). In the white and Ni-free clay sample (BONBR2c), the 3697 cm^{-1} and 3650 cm^{-1} bands of the MIR spectrum belong to serpentine species (Figure

4a). They were assigned respectively to the inner OH stretching and the out-of-phase vibrations of the inner-surface OH of lizardite (Balan et al. 2002). In the same spectrum, the band at 3677 cm^{-1} can be assigned to OH stretching vibrations in νMg_3OH configuration of TL (e.g. Baron et al. 2016). These assignments imply that the bands observed at 7239 cm^{-1} and 7185 cm^{-1} in the NIR spectrum of BONBR2c correspond to second overtone vibrations ($2\nu Mg_3OH$) in SL and TL minerals, respectively. The other bands reported at lower frequencies on the MIR and NIR spectra of the four bluish green clay samples (BONBR2A, MG3aWil, LFSTA5a2 and MG1aWil) most likely result from additional occurrence and distinct distribution of Ni in octahedral sheets of these layers silicates. More specifically, the 3628 cm^{-1} (MIR – Figure 4a) and 7081 cm^{-1} (NIR – Figure 4b) bands are respectively assigned to first and second overtones Ni_3OH stretching for TL minerals and trioctahedral smectites (Farmer, 1974; Gerard and Herbillon, 1983; Petit, 2005; Christidis and Mitsis, 2006; Jagannadha Reddy et al., 2009; Mano et al., 2014; Baron and Petit, 2016; Baron et al., 2016). The 3650 cm^{-1} (MIR – Figure 4a) and 7125 cm^{-1} (NIR – Figure 4b) bands can also be attributed to first and second overtones $MgNi_2OH$ stretching for TL minerals (Petit et al., 2004; Baron and Petit, 2016). As highlighted by Fritsch et al. (2019), these results suggest that TL minerals (and/or trioctahedral smectite) are the main Ni-bearing phases of the Ni-silicate ores. Nevertheless, the bands at 3650 cm^{-1} (MIR) and 7125 cm^{-1} (NIR) could also be assigned to νNi_3OH in serpentine (Baron et al. 2016). These bands are commonly poorly resolved, except for sample MG1aWill, which could therefore contain Ni-rich SL minerals (Nepouite) in addition to Ni-rich TL minerals (Pimelite).

Chemical compositions

Bulk chemical compositions of the five samples (expressed in oxide weight %) are listed in Table 1. These layer silicates are mainly composed of Si with minor Fe, highly variable Mg,

and Ni contents (or reverse Mg and Ni variations), and are free of Al. Bulk chemical data converted to numbers of atoms and plotted in a ternary Si/(Mg+Fe)/Ni diagram (Figure 5) reveal that all five samples are within a triangle delineated by the Mg/Fe end-member of serpentine species (Srp), and the Mg and Ni end-members of talc (Tlc). As outlined by Fristch et al. (2016; 2019), the relative proportion of TL minerals in mixtures of both 7 Å and 10 Å layer silicates can be assessed from the mole Si:ΣR ratio (with ΣR = Mg+Fe+Ni). This ratio is shown on the ternary diagram by a horizontal line. Theoretically, it ranges from 2/3 for samples composed exclusively of serpentine species [$R_3Si_2O_5(OH)_4.nH_2O$] to 4/3 for those composed only of 2:1 layer silicates in the talc mineral group [$R_3Si_4O_{10}(OH)_2$] (see the two horizontal solid lines in Figure 5). The ternary Si/(Mg+Fe)/Ni diagram shows, therefore, that the five samples present dominant TL minerals in the mixture of 7 Å and 10 Å layer silicates, which is consistent with Si:ΣR ratios greater than 1.00. This is also consistent with XRD patterns showing a major contribution of the basal reflections of the 2:1 layer silicates compared to those of the 1:1 layer silicates (Figure 3). Samples with the highest Si/ΣR ratios and lowest Fe contents (Table 1) are predominantly made of TL minerals and are, therefore, the closest to the theoretical line for talc on the ternary diagram. This is the case for samples MG1aWill and MG3aWill. The presence of quartz in MG1aWill, in addition to TL minerals, as revealed by XRD, may also increase the Si/ΣR and thus induce an overestimation of the proportion of TL minerals. Major chemical changes are related to a right shift of the data from the Mg+Fe pole to the Ni pole of the ternary diagram. In agreement with our IR data, this shift points to a gradual increase of the Ni for Mg substitution in the layer silicates (mostly TL minerals) of the infillings. This substitution rate is nil in the most expandable sample (BONBR2c) and optimal in the less expandable sample (MG1aWill).

Swelling and shrinking behavior

XRD patterns of oriented mounts of the < 2 µm fractions of the five samples saturated with Ca or Li in AD and EG states are given in Figure 6. XRD patterns of the Ca-saturated samples in AD state are very similar to those of the powder bulk samples (Figure 3). They all present similar peaks with broadened *00l* reflections characteristic of poorly crystalline 1:1 (SL) and 2:1 (TL) layer silicates. The position of the *001* reflection of the 2:1 layer silicates in AD state ranges from 9.92 Å (MG1aWill) to 10.20 Å (BONBR2c) for the Ca-saturated samples (Figure 6a, Table 2) and from 9.92 Å (MG1aWill) to 10.82 Å (BONBR2c) for the Li-saturated samples (Figure 6b, Table 2). The position of this reflection at about 10 Å is slightly greater than that generally reported 9.6 Å for non-expandable TL minerals (Brindley et al., 1977; Brindley and Brown, 1980).

XRD patterns of the Ca or Li-saturated samples in EG state (Figure 6) show no significant change in peak position for the 1:1 layer silicates (Srp and SL), indicating an absence of swelling phase (Figure 6). The *001* reflection of the 2:1 layer silicates for MG1aWill is at the same position (~10 Å) in the AD and EG states, confirming also the absence of swelling phase (Figures 6 and 7; Table 2). The most expandable sample (BONBR2c) exhibits a *001* peak of 16.47 Å for CaEG and 17.04 Å for LiEG, and a *002* peak of ~ 8.80-8.90 Å for CaEG and LiEG (Figures 6 and 7; Table 2). These harmonic peaks are close to that reported by Christidis and Mitsis (2006) for stevensite (respectively 17.6 Å and ~ 9.02 Å). The other samples have intermediate amounts of expandable and non-expandable layers, according to the position of the first basal reflection between 10 and 17 Å in EG state. Figures 6a and 6b also show that EG solvation of the two most expandable samples, BONBR2a and BONBR2c, saturated with Li^+ leads to better resolved reflections, as well as to larger shifts of the peaks towards low angles (i.e. larger d-spacings) than for samples saturated with Ca (Table 2). Such differences likely result from the smaller size of Li^+ and different ionic potential compared to Ca^{2+}, implying different solvation behaviours with water or ethylene glycol.

The swelling and the splitting of the *001* reflection in samples BONBR2a, BONBR2c and MG3aWill are better illustrated in background stripped patterns (Figure 7). The asymmetric *001* reflection at ~10.0 Å for the 2:1 layer silicates in AD state (dots in Figure 7) can be fitted with two overlapping Gaussian curves (dashed lines, Figure 7). The peak asymmetry disappears with EG solvation and is replaced by two contributions, which are fitted with two separate Gaussian curves (plain line). From Figures 7c to 7b to 7a, the increase in the swelling ability of the three samples is linked to a shift of the first contribution (P1) towards low angles (14.15 Å for MG3aWill, 15.27 Å for BONBR2c and 17.04 Å for BONBR2a) with a concomitant increase of the peak area. In contrast, the second contribution (P2) shifts towards high angles (9.44 Å for MG3aWill, 9.24 Å for BONBR2a and 8.83 Å for BONBR2c), and gradually decreases. These variations suggest a random interstratification (R0) between swelling (smectite) and non-swelling phases (TL) with a variable proportion of the two components.

Figure 8 displays the positions of both contributions (P1 and P2) for the five Ca- and Li-saturated samples in EG state. The progressive variation of the P1 and P2 positions from samples MG1aWill to BONBR2c suggests a continuum between the non-expandable TL and the fully expandable smectite. It also shows that the P1 and P2 positions are negatively correlated and that non-expandable TL minerals and stevensite are at the extremities of the trend. More specifically, P1 and P2 are merged and located close to the *001* reflection of the non-expandable TL minerals (corresponding to a d-spacing of ~ 9.6 Å) in the non-swelling sample (MG1aWill) and widely separated and positioned close to the *001* (P1) and *002* (P2) reflections of stevensite (d-spacings close to 17.6 Å and 8.8 Å, respectively) in the highly swelling sample (BONBR2c). Accordingly, the positions of both reflections (P1 and P2) could be used to assess the relative proportion of swelling layers (stevensite) in the mixture of the 2:1 layer silicates.

Following K-saturation and gradual heating from room temperature to 550 °C, the *001* reflection of TL was displaced from 10.0-9.9 Å to 9.6-9.7 Å (Figure 9). Simultaneously, the intensity and width of the 001 peaks, as well as their asymmetry on the low angle side, decreased with increasing temperature for all samples except MG3aWILL. These variations indicate a preferential collapse of the swelling (or hydrated) layers of these clay minerals. The position of the *001* reflection at ~9.6 Å after heating and the destruction of the swelling layers therefore reveal the non-expandable TL minerals (Brindley et al., 1977, Brindley and Brown, 1980). At 550 °C the collapse of the *001* reflection is complete for serpentine (thermal dehydroxylation of Srp and SL minerals) whereas it remains partial for TL minerals.

Layer charge and vacancies

XRD patterns of the Li-saturated samples after heating at 300 °C (Hofmann Klemen treatment) show a peak displacement from 10.87 Å (LiAD) to 10.44 Å (Li_{300}) for BONBR2c and from 10.07 Å (LiAD) to 9.93 Å (Li_{300}) for MG1aWill (Li_{300}, Figure 6b). For the five samples the intensity decrease is related to the proportion of swelling layers. Following EG solvation after HK treatment (Li_{300EG} Figure 6b) the 001 and 002 peaks are broad and hardly discernible from the background for samples BONBR2a, BONBR2c and LFSTA5a2, and their position ranges from ~15 Å to ~ 17 Å and from ~ 9.4 Å to ~ 8.8 Å, respectively. This behaviour indicates that the layer charge is partially neutralised by migration of Li^+ ions toward vacant sites upon HK treatment, and thus that it originates from the octahedral sheet.

The comparison of the FTIR NH_4 band before and after the HK treatment (i.e. NH_4^+-saturated samples previously saturated with Li and heated at 300 °C: $Li_{300}NH_4$) reveals a charge loss that ranges from 63% in the highly expandable sample (BONBR2c) to 39% in the non-expandable one (MG1aWill; Table 3). Upon Li-saturation the samples with the highest swelling ability show the largest charge loss, whereas those with the lowest swelling capacity

This is a preprint, the final version is subject to change, of the American Mineralogist (MSA)
Cite as Authors (Year) Title. American Mineralogist, in press.
DOI: https://doi.org/10.2138/am-2020-6984

show the lowest loss of charge neutralised by Li^+. The swelling ability is thus correlated with the amount of charge neutralised by Li^+ and hence with the amount of octahedral vacancies. The swelling components of these samples can thus be identified as trioctahedral 2:1 layers with octahedral vacancies, and therefore as stevensite layers. The decrease in swelling ability after HK treatment indicates a loss of layer charge due to partial neutralisation of the charge of the stevensite by Li^+ after heating. This is consistent with what is expected for trioctahedral smectites with octahedral charge where Li-saturation followed by heating (HK treatment) induces partial neutralisation of approximately half of the charge (Li^+ vs. R^{2+}; Petit et al., 2008).

DISCUSSION AND CONCLUSIONS

Swelling capacity and octahedral vacancies of hydrous Mg/Ni layer silicates

The occurrence of the hydrous Mg/Ni layer silicates in clay infillings of faulted peridotites have recently been linked to the early alteration of serpentine veins and conversion of serpentine species into cryptocrystalline SL residues and newly formed TL minerals (Fritsch et al., 2016). These tri-octahedral layer silicates of the serpentine and talc groups have often been considered as non-expandable, and the occurrence of swelling layers (i.e. stevensite) has scarcely been reported worldwide (Christidis and Mitsis, 2006; Capitani and Ventruti, 2018). Our work suggests that such occurrence could be more common than initially thought. Based on XRD and FTIR analyses of the saturated clay samples (Ca^{2+}, Li^+, NH_4^+, K^+) subjected to or not to ethylene glycol and heat treatments, we have linked the swelling capacity of these samples to the content of stevensite layers (or octahedral vacancies) from the 2:1 layer silicates of the clay infillings.

In the XRD patterns of Ca- or Li-saturated and air-dried clay samples, swelling of the 2:1 layer silicates causes *001* peak shifts towards low angles (or development of peak asymmetry or a shoulder on the low angle slopping side of the peak), and splitting of this peak into two contributions (P1 and P2) after solvation of the saturated clay samples with ethylene glycol. The split increases with the swelling capacity of the samples. It is nil (P1 = P2) for samples composed of non-expandable TL minerals (*001* peak close to 9.6 Å) and the largest for samples composed exclusively of stevensite (P1: *001* peak at ~ 17.0 Å, P2: *002* peak at ~ 8.8). Intermediate values between these two ends (Figure 8), together with considerable peak broadening and the occurrence of irrational basal reflections, suggest the presence of random interstratification (R0) between non-expandable TL and expandable stevensite. These intermediate values could also be due to three-component mixed layers (Figure 10) including non-expandable TL layers, partially expanded stevensite (one sheet of EG), and fully expanded stevensite (two sheets of EG) (Eberl et al., 1982; Christidis and Eberl, 2003).

In this study we also closely linked the swelling behaviour of the clay infillings to layer charge and octahedral vacancies in the 2:1 layer silicates (Hofman Klemen test). As illustrated in Figure 10, the larger d-spacings (or hydration) of stevensite layers originate from larger numbers of vacant sites in the octahedral sheets and divalent cations (Mg^{2+}, Ni^{2+}) in the interlayer spaces. The non-expandable layers with a low charge are assigned to TL (Si_4[Mg, Ni]$_3O_{10}(OH)_2$, nH_2O) (Figure 10a). Conversely, the fully expandable layers with a higher charge and optimum octahedral vacancies are assigned to stevensite ($(Mg^{2+},Ni^{2+})_xSi_4[Mg,Ni]_{3-x}\square_xO_{10}(OH)_2 \cdot nH_2O$ with □ being a random vacancy) (Figures 10 b and c). In the stevensite structure, a fraction of divalent cations (Mg^{2+} and Ni^{2+}) no longer occupy octahedral sites, but situate over inter-layer positions (exchangeable cation). Petit et al. (2008) showed for synthetic Zn-stevensite that the layers having a charge < ~0.2 (per half

unit cell) are non-expandable while those having a charge > ~0.2 can swell upon ethylene glycol solvation.

The proportion of Ni in the octahedral sheets of the 2:1 layer silicates (or Ni for Mg substitution rate) does not seem to affect the swelling capacity of these minerals. Although the richest Ni-sample (MG1aWill) contains only non-expandable TL and the Ni-free sample (BONBR2c) contains mostly stevensite, the relationship between the Ni for Mg substitution rate and swelling capacity of the 2:1 layer silicates is not as evident as with other samples (BONBR2A, MG3aWil, LFSTA5a2). On the other hand, Fritsch et al. (2019) reported an opposite trend based on the relationship established from thin sections between the Ni content and anisotropy of the TL infillings. Indeed Mg-rich domains in these clay infillings (kerolite) are commonly anisotropic and occur as botryoidal-shaped ribbons, whereas Ni-rich domains of the same infillings (pimelite) are optically isotropic and cryptocrystalline. This observation suggests greater amounts of crystal defects (including octahedral vacancies) in pimelite (Ni-rich) compared to kerolite (Mg-rich), which is supported by the more extensive development of cracks in the Ni-rich parts (or bands) of the TL infillings, as observed in thin sections (Figure 2d). To better establish the relationships between Ni for Mg substitution and vacancies in TL minerals , further investigation should be undertaken on a larger set of clay infillings.

Formation conditions of hydrous Mg/Ni layer silicates

Recent studies on clay infillings (deweylite/garnierite) in reactivated faults of peridotite formations from New Caledonia have suggested the contribution of temperature and pressure (i.e. hydrothermal processes) in the alteration of serpentine veins into clay infillings predominantly made of TL minerals (Fritsch et al., 2016, 2019; Cathelineau et al., 2017). More specifically, Fritsch et al. (2019) emphasised that temperature in the clay infillings

could have affected the size and crystallinity of the 2:1 layer silicates that we assign in this work to TL minerals, interstratified TL/stevensite and stevensite. On the other hand, laboratory experiments carried out by Decarreau et al. (1987) showed that the stability fields of talc, kerolite and Mg or Ni-stevensite are temperature-dependent. Stevensites can be synthesised below 100 °C, kerolites between 100 and 170 °C, and talc above 500 °C. We conclude that the proportion of stevensite (or vacant sites) in 2:1 layer silicates could be used as an efficient means for assessing their formation temperature. Vein infillings exclusively composed of non-expandable TL as 2:1 layer silicates would have precipitated well above 100 °C, whereas those composed of almost pure stevensite would have formed below that temperature (i.e. closer to ambient temperature). This interpretation suggests that temperature could have controlled the distribution of non-expandable TL and expandable stevensite along reactivated faults during early alteration of the peridotite formations. Both mineral phases would have precipitated simultaneously but at different places along the fault network. However, stevensite could also have been produced later during the interaction of meteoric fluids with faulted peridotites and the development of thick lateritic profiles by weathering and hydration of TL minerals into poorly ordered and highly swelling smectite.

Some possible technological implications

Nickel is widely used in industry, because of its unique chemical and physical properties and resistance to corrosion, for the production of stainless steel and alloys (~81% of Ni consumption; Schnebele 2017), plating (~7% of Ni consumption; Schnebele 2017) and 12% for other uses (Schnebele 2017) including the production of electric batteries, and to a lesser extent (a few %) as a catalyst. The demand for Ni increases at a rate of ~4 % per year and it will continue to rise in the future with the development of electrical vehicle/batteries. Nickel

476 is mainly exploited from sulphide and lateritic ores which respectively correspond to 30-40%
477 and 60-70% of the world resource (Schnebele 2017). Sulphide ores with high Ni grades have
478 been the dominant source of Ni because the processing is simpler and cheaper than for
479 laterites. In recent years, the proportion of Ni extracted from sulphide ores gradually
480 decreased (currently 60-65% of Ni production) with the rarefaction of these deposits
481 (Bergmann, 2003; Gleeson, et al., 2003; Dalvi et al., 2004; Butt and Cluzel, 2013), while that
482 of lateritic ores increased (currently 35-40% of Ni production) and will continue to rise.
483 Because of the progressive decrease in the Ni grade of available laterite ores, and the needs to
484 address related environmental issues and to develop economically feasible co-exploitation
485 strategies of associated trace metals (e.g. Co in limonitic ores), industrial processes of Ni
486 extraction are becoming more and more complex. Pyrometallurgical processes are
487 predominant for sulphides but the use of hydrometallurgical processes, such as Acid Leaching
488 (AL) or High-Pressure Acid Leaching (HPAL), is increasing for both sulphide and laterite
489 ores (Diaz et al., 1998, McDonald and Whittington, 2008; Rice, 2016; Ucyildiz and Girgin,
490 2017, Mano et al., 2019). These processes are more efficient for low-grade ores and have
491 better recoveries of Ni and other metals. To improve these processes, detailed knowledge of
492 the mineralogy and crystal chemistry of Ni-bearing clay silicates is essential for economically
493 viable (Ni recovery) and environmentally sustainable (acid consumption) Ni mining.
494 There is also an increasing interest in the use of Ni-bearing phyllosilicates as catalysts
495 because Ni is one of the most active metals for the dry reforming of methane (activation of C-
496 H bond) and the cleavage of C-C bonds (Wang et al., 1998; Vogels et al., 2005; Iwasa et al.
497 2006; Sivaiah et al., 2010; Yoshida et al. 2015; Akri et al., 2017). The Ni-bearing clays occur
498 naturally and can be easily synthesised (Iwasa et al. 2006, Baron et al., 2016). The Ni-based
499 catalysts are reduced to produce active metal Ni in the temperature range 500-800 °C. The Ni
500 content of Ni-phyllosilicates, their crystal chemistry characteristics (octahedral vs.

exchangeable Ni) and excellent stability at high temperature are key factors in affecting their catalytic efficiency.

ACKNOWLEDGEMENTS

The authors thank Fabien Trotet, Pierre Epinoux, Philippe Bains, Philippe Hoffler, Gilles Monteil (SLN), Julie Michaud (SMT/SMCB), Yann Dijkstra, René Feré (CFTMC), Clément Couteau, Frédéric Villedieu (KNS) and Christian Tessarolo (Goro-VALE) who provided helpful technical reports and assistance for access to mining sites. The authors gratefully acknowledge the associate editor, and the two reviewers, G. Christidis and an anonymous reviewer, for their constructive comments, which allowed significant improvement of the manuscript. This research was funded by the projects “Conditions of formation of Mg/Ni silicate ores from New Caledonia” (2010, INSU CESSUR) and “Ni/Co mineralisation factors of laterites derived from ultramafic rocks of New-Caledonia” (2010-2014, CNRT Nickel and its environment). The authors acknowledge financial support from the European Union (ERDF) and "Région Nouvelle Aquitaine".

REFERENCES

Akri M., Pronier S., Chafik T., Achak O., Granger P., Simon P., Trentesaux M. and Batiot-Dupeyrat C. (2017) Development of nickel supported La and Ce-natural illite clay for autothermal dry reforming of methane: Toward a better resistance to deactivation. Applied Catalysis B: Environmental, 205, 519–531

Balan, E., Saitta, A.M., Mauri, F., Lemaire, C. and Guyot, F. (2002) First-principles calculation of the infrared spectrum of lizardite. American Mineralogist, 87, 1286–1290.

526 Baron, F., Pushparaj, S.S.C., Fontaine, C., Sivaiah, M.V., Decarreau, A., Petit, S. (2016)
527 Microwave-assisted hydrothermal synthesis of Ni-Mg layered silicate clays. Current
528 Microwave Chemistry, 3, 85–89.
529 Baron, F. and Petit, S. (2016) Interpretation of the infrared spectra of the lizardite-nepouite
530 series in the near-and mid-infrared range. American Mineralogist, 101, 423–430.
531 Bergman, R.A. (2003) Nickel Production from Low-Iron Laterite ores: process Description.
532 CIM Bulletin, 96, 127–138.
533 Bish D. L. and Brindley G. W. (1978) Deweylites, mixtures of poorly crystalline hydrous
534 serpentine and talc-like minerals. Mineralogical Magazine, 42, 75–79.
535 Brand, N.W., Butt, C.R.M. and Elias, M. (1998) Nickel laterites: classification and features.
536 AGSO Journal of Australian Geology and Geophysics, 17, 81–88.
537 Brindley, G.W. (1980): The structure and chemistry of Hydrous Nickel-containing silicate
538 and Nickel-Aluminium Hydroxy minerals. Bulletin de Minéralogie, 103, 161–169.
539 Brindley G.W. and Hang P. T. (1973) The nature of garnierites-I: Structures, chemical
540 compositions and color characteristics. Clays and clays minerals, 21, 27–40.
541 Brindley G.W., Bish D. L. and Wan H. M. (1977) The nature of kerolite, its relation to talc
542 and stevensite. Mineralogical magazine, 41, 443–452.
543 Brindley G.W. and Wan H.M. (1979) Compositions, structures, and properties of nickel-
544 containing minerals in the kerolite-pimelite series. American Mineralogist, 64, 615–625.
545 Brindley G.W. and Brown, G. (1980) Crystal structures of clay minerals and their X-ray
546 identification. Mineralogical society, London, 494 p.
547 Butt C.R.M. and Cluzel D. (2013) Nickel Laterite Ore Deposits: Weathered Serpentinites.
548 Elements, 9, 123–128

549 Capitani, G.C. and Ventruti, G. (2018) Ni-serpentine nanoflakes in the garnierite ore from
550 Campello Monti (Strona Valley, Italy): Népouite with some pecoraite outlines and the
551 processing of Ni-containing ore bodies. American Mineralogist, 103, 629–644.
552 Cathelineau, M., Myagkiy, A., Quesnel, B., Boiron, M.C., Gautier, P., Boulvais, P., Ulrich,
553 M., Truche, L., Golfier, F., Drouillet, M. (2017) Multistage crack seal vein and
554 hydrothermal Ni enrichment in serpentinised ultramafic rocks (Koniambo massif, New
555 Caledonia). Mineral. Depos., 52, 961–978.
556 Christidis G. E. and Mitsis I. (2006) A New Ni-rich stevensite from the ophiolite complex of
557 Othrys, central Greece. Clays and Clay Minerals, 54, 653–666.
558 Cluzel D., 2006. Synthèse géologique de la Nouvelle-Calédonie et de sa zone économique
559 exclusive. Rapport de synthèse de la convention ISTO-IFREMER, programme
560 EXTRAPLAC.
561 Cluzel, D. and Vigier, B. (2008) Syntectonic mobility of supergene nickel ores from New
562 Caledonia (Southwest Pacific). Evidences from faulted regolith and garnierite veins.
563 Resource Geology, 58, 161–170.
564 Dalvi, A., Bacon, G. and Osborne, R. (2004) The past and the future of nickel laterites. In:
565 PDAC 2004 International convention, Toronto, Canada. Trade show and investors
566 exchange. Toronto: Prospectors and Developers Association of Canada, 7–10.
567 Decarreau, A., Colin, F., Herbillon, A., Manceau, A., Nahon, D., Paquet, H., Trauth-Badaud,
568 D., and Trescases, J. J. (1987) Domain segregation in Ni-Fe-Mg-smectites: Clays and
569 Clay Minerals, 35, 1–10.
570 Diaz, M.C., Landolt, C.A., Vahed, A., Warner, A.E.M. and Taylor, J.C. (1988) A review of
571 nickel pyrometallurgical operations. Journal of metals, 40, 9, 28–33.
572 Eberl, D.D. Jones, B.F. and Khoury, H.N. (1982) Mixed-layer kerolite/stevensite from the
573 Amargosa Desert, Nevada. Clays and Clay Minerals, 30, 321–326.

574 Farmer, V.C. (1974) The Infrared Spectra of Minerals, 539 p. The Mineralogical Society,
575 London.
576 Faust, G.T. (1966) The hydrous nickel-magnesium silicates - The garnierite group. American
577 Mineralogist, 51, 279–298.
578 Faust G.T. and Murata K.J. (1953) Stevensite, redefined as a member of the montmorillonite
579 group. American Mineralogist, 38, 973–987.
580 Freyssinet, P., Butt, C.R.M., Morris, R.C. and Piantone, P. (2005) Ore-forming processes
581 related to lateritic weathering. In: Hedenquist JW, Thomson JFH, Goldfarb RJ, Richards
582 JP (eds), Economic Geology 100th Anniversary Volume. Economic Geology Publishing
583 Company, New Haven, Connecticut, 681–722.
584 Fritsch, E., Juillot, F., Dublet, G., Fonteneau, L., Fandeur, D., Martin, E., Caner, L., Auzende,
585 A.L., Grauby, O. and Beaufort. D. (2016) An alternative model for the formation of
586 hydrous Mg/Ni layer silicates (‘deweylite’/‘garnierite’) in faulted peridotites of New
587 Caledonia: I. Texture and mineralogy of a paragenetic succession of silicate infillings.
588 European Journal of Mineralogy, 28, 295–311.
589 Fritsch, E.J.C., Juillot, F., Dublet, G., Fonteneau, L., Fandeur, D., Martin, E., Caner, L.,
590 Auzende, A.L. and Beaufort. D. (2019) An alternative model for the formation of
591 hydrous Mg/Ni layer silicates (“deweylite”/“garnierite”) in faulted peridotites of New
592 Caledonia: II. Petrography and chemistry of white and green clay infillings. European
593 Journal of Mineralogy, 31, 945–962.
594 Gaudin A., Grauby O., Noack N., Decarreau A. and Petit S. (2004) Accurate crystal chemistry
595 of ferric smectites from the lateritic nickel ore of Murrin Murrin (Western Australia). I.
596 XRD and multi-scale chemical approaches. Clay Minerals, 39, 301–315.
597 Gerard P. and Herbillon A.J. (1983) Infrared studies of Ni-bearing clay minerals of the
598 kerolite-pimelite series. Clays and Clays minerals, 31, 143–151.

599 Gleeson S.A., Butt C.M.R. and Elias M. (2003) Nickel laterites: a review. SEG Newsletter,
600 Society of Economic Geology, 54, 9–16.
601 Gleeson, S.A., Herrington, R.J., Durango, J., Velasquez, A. an Koll, G. (2004) The
602 Mineralogy and Geochemistry of the Cerro Matoso S.A. Ni Laterite Deposit,
603 Montelibano, Colombia. Economic Geology, 99, 1197–1213.
604 Greene-Kelly, R. (1953) Irreversible dehydration in montmorillonite. Part II. Clay Minerals
605 Bulletin. 1, 52–56.
606 Greene-Kelly, R. (1955) Dehydration of montmorillonite minerals. Mineralogical Magazine,
607 30, 604–615.
608 Hofmann, U. and Klemen, R. (1950) Verlust der austausehfahigkeit von lithiumionen an
609 Bentonit durch Erhitzung. Zeitschrift für Anorganische und Chemie, 262, 95–99.
610 Iwasa N., Takizawa M. and Arai M. (2006) Preparation and application of nickel-containing
611 smectite-type clay materials for methane reforming with carbon dioxide. Applied
612 Catalysis A: General, 314, 32–39
613 Jagannadha Reddy, B., Frost, R. L. and Dickfos, M. J. (2009) Characterisation of Ni silicate
614 bearing minerals by UV–vis–NIR spectroscopy - Effect of Ni substitution in hydrous Ni–
615 Mg silicates. Spectrochimica Acta, Part A, 1762–1768.
616 Manceau A. and Calas G. (1985) Heterogeneous distribution of nickel in hydrous silicates
617 from New Caledonia ore deposits. American Mineralogist, 70, 549–558.
618 Mano, E.S., Caner, L., Petit, S., Chaves, A.P. and Mexias, A.S. (2014) Mineralogical
619 characterisation of Ni-bearing smectites from Niquelândia, Brazil. Clays and Clay
620 Minerals, 62, 324–335.
621 Mano, E.S., Caner, L., Petit, S., Chaves A. P. and Mexias, A.S. (2019) Ni-smectitic ore
622 behaviour during the Caron Process. Hydrometallurgy, 186, 200–209.

McDonald R.G. and Whittington B.I. (2008) Atmospheric acid leaching of nickel laterites review Part I. Sulphuric acid technologies. Hydrometallurgy, 91, 35–55.

Pecora W.T., Hobbs S.W. and Muraxa K.J. (1949) Variations in garnierite from the nickel deposit near Riddle, Oregon. Economic Geology, 44, 13–23.

Petit, S. (2005) Crystal-chemistry of talcs: a NIR and MIR spectroscopic approach. In: J.T. Kloprogge, (Ed.), The Application of Vibrational Spectroscopy to Clay Minerals and Layered Double Hydroxides: CMS Workshop Lectures, Aurora, Colorado. 13, 41–64.

Petit, S., Righi, D., Madejová, J. and Decarreau, A. (1998) Layer charge estimation of smectites infrared spectroscopy. Clay Minerals, 33, 579–591.

Petit, S., Caillaud, J., Righi D., Madejová, J., Elsass, F. and Köster, H.M. (2002) Characterisation and crystal chemistry of an Fe-rich montmorillonite from Ölberg, Germany. Clay Minerals, 37, 283–297.

Petit, S., Martin, F., Wiewióra, A., De Parseval, P. and Decarreau, A. (2004) Crystal-chemistry of talc: a near infrared (NIR) spectroscopy study. American Mineralogist, 89, 319–326.

Petit, S., Righi, D. and Madejová, J. (2006) Infrared spectroscopy of NH_4^+-bearing and saturated clay minerals: A review of the study of layer charge. Applied Clay Science, 34, 22–30.

Petit, S., Righi, D. and Decarreau, A. (2008) Transformation of synthetic Zn-stevensite to Zn-talc induced by the Hofmann-Klemen effect. Clays and Clay Minerals, 57, 645–654.

Proenza, J.A., Lewis, J.F., Galí, S., Tauler, E., Labrador, M., Melgarejo, J.C., Longo, F., Bloise, G. (2008): Garnierite mineralisation from Falcondo Ni-laterite deposit (Dominican Republic). Macla, 9, 197–198.

Rice, N. M. (2016) A hydrochloric acid process for nickeliferous laterites. Minerals Engineering, 88, 28–52.

Schnebele E. K. (2017) U.S. Geological Survey, Mineral Commodity Summaries. 206p.

Sivaiah, M.V.. Petit, S. Barrault, J. Batiot-Dupeyrat, C. and Valange, S. (2010) CO_2 reforming of CH_4 over Ni-containing phyllosilicates as catalyst precursors. Catalysis Today, 157, 397–403.

Tauler, E., Proenza, J.A., Galí, S., Lewis, J.F., Labrador, M., García-Romero, E., Suárez, M., Longo, F., Bloise, G. (2009) Ni-sepiolite-falcondoite in garnierite mineralisation from the Falcondo Ni-laterite deposit, Dominican Republic. Clay Minerals, 44, 435–454.

Ucyildiz A. and Girgin I. (2017) High pressure sulphuric acid leaching of lateritic nickel ore. Physicochemical Problems of Mineral Processing, 53, 475−488

Villanova-de-Benavent, C., Proenza, J.A., Galí, S., García-Casco, A., Tauler, E., Lewis, J.F. and Longo, F. (2014) Garnierites and garnierites: Texture, mineralogy and geochemistry in the Falcondo Ni-laterite deposit, Dominican Republic. Ore Geology Reviews, 58 C, 91–109.

Vogels R.J.M.J., Kloprogge J.T. and Geus J.W. (2005) Catalytic activity of synthetic saponite clays: effects of tetrahedral and octahedral composition. Journal of Catalysis, 231, 443-452.

Wang S., Zhu H.Y. and Lu G. Q. (1998) Preparation, Characterization, and Catalytic Properties of Clay-Based Nickel Catalysts for Methane Reforming. Journal of Colloid and Interface Science, 204, 128–134

Wells, M.A., Ramanaidou, E.R., Verrall, M. and Tessarolo, C. (2009) Mineralogy and crystal chemistry of ‘‘garnierites’’ in the Goro lateritic nickel deposit, New Caledonia. European Journal of Mineralogy, 21, 467–483.

Wiéwióra A., Dubinska E. and Iwasinska I. (1982) Mixed-layering in Ni-containing talc-like minerals from Szklary, Lower Silesia, Poland. Proceedings of the International Clay Conference, Pavia, Italy, 111–125.

673 Wojdyr, M. (2010) Fityk: a general-purpose peak fitting program: Journal of Applied
674 Crystallography, 43, 1126-1128.
675 Yoshida H., Watanabe K., Iwasa N., Fujita S. and Arai M. (2015) Selective methanation of
676 CO in H_2-rich gas stream by synthetic nickel-containing smectite based catalysts. Applied
677 Catalysis B: Environmental 162, 93–97
678

This is a preprint, the final version is subject to change, of the American Mineralogist (MSA)
Cite as Authors (Year) Title. American Mineralogist, in press.
DOI: https://doi.org/10.2138/am-2020-6984

679

680

681 **Figure captions**

682 **Figure 1**: Peridotite formations of New Caledonia and the locations of our sampling sites for
683 the Mg/Ni silicate ores of the Koniambo and Poro massifs (arrows).

684

685 **Figure 2**: **(a)** General view of reactivated cross-cutting faults with white (Dew: deweylite)
686 and bluish green (Gar: garnierite) coatings (or infillings) along black serpentine network of
687 saprock (SR_{Hz}) of thick Ni-lateritic profiles (Poro, Fatma), **(b)** Close-up of **(a)** showing olive
688 green (STL) and turquoise (TL) infillings of a garnierite vein (Gar) with numerous cracks
689 (note also at the periphery of the vein remains of black serpentines and in its central part a
690 thin white silica infilling, Qz), **(c)** Densely cracked turquoise (sample BONBR2a) and white
691 infillings (sample BONBR2c) along serpentine veins (Srp) of hazburgite saprolite (SAP_{Hz}),
692 **(d)** BSE image of a garnierite vein showing the whole sequence of clay (STL, TL) and silica
693 (Qz) infillings. In this vein, the development of cracks (due to drying) is mostly observed in
694 the Ni-rich (light grey) part of the TL infilling.

695

696 **Figure 3**: XRD patterns of randomly oriented powders of the five samples showing broad
697 diffraction peaks of the serpentine-like (SL – 1:1) and talc-like (TL – 2:1) mineral phases and
698 sharp and smaller peaks for residual serpentine species (Srp: mainly lizardite Lz and
699 chrysotile Ctl) and quartz (Qz).

700

701 **Figure 4**: FTIR spectra of the < 2 μm fractions of the five samples **(a)** in the OH-stretching
702 region (Middle Infrared) and **(b)** in the first OH overtone region (Near Infrared) of the 1:1 and
703 2:1 layer silicates.

This is a preprint, the final version is subject to change, of the American Mineralogist (MSA)
Cite as Authors (Year) Title. American Mineralogist, in press.
DOI: https://doi.org/10.2138/am-2020-6984

704

705

706 **Figure 5**: Plots of the molar chemical compositions of the five samples (arrows) (see also
707 Table 1 for the chemical compositions of the five samples in oxides wt %) in a ternary Si *vs*
708 Mg+Fe *vs* Ni diagram, together with those of Mg/Ni layer silicates of the serpentine (Srp)
709 and talc (Tlc) groups from New Caledonia, investigated by Fritsch et al. (2016, 2019).

710

711 **Figure 6**: XRD patterns of oriented mounts of the five clay samples after Ca saturation (a)
712 and Li saturation (b) in the air-dried (AD) and ethylene glycol solvated (EG) states. Plain line:
713 CaAD or LiAD; dashed line: CaEG or LiEG. In (b), two additional XRD patterns per sample
714 are shown: dotted line - Li_{300}: after heating at 300 °C (Hofman Klemen treatment); dash-
715 dotted line - Li_{300}EG: after heating at 300 °C and solvation with EG.

716

717

718 **Figure 7**: Deconvolution of XRD peaks of Li saturated clay fractions in AD and EG states of
719 the three most expandable samples (MG3aWill, BONBR2a and BONBR2c) in the 2θ range 3-
720 13° after background stripping. Dots: experimental data; solid lines: best fit; dashed lines:
721 Gaussian contributions (in the EG state the Gaussian contribution is identical to the best fit).

722

723 **Figure 8**: Relation between the d-spacing of the low angle peak (P1: 4-7° 2θ) and that of the
724 high angle peak (P2: 7-10° 2θ) of the 2:1 layer silicates in CaEG and LiEG states, determined
725 from XRD peak deconvolution of the most swelling samples (MG3aWill, BONBR2a and
726 BONBR2c).

727

This is a preprint, the final version is subject to change, of the American Mineralogist (MSA)
Cite as Authors (Year) Title. American Mineralogist, in press.
DOI: https://doi.org/10.2138/am-2020-6984

728 **Figure 9:** XRD patterns of oriented mounts of the five clay samples saturated with K at room
729 temperature (AD 20°C, solid line) and after heating at 150 °C (dashed line), 350 °C (doted
730 line) and 550 °C (dash-doted line).

731

732 **Figure 10:** Structures of the three components (a-TL, b-partly expanded stevensite and c-fully
733 expanded stevensite) of the interstratified 2:1 layer silicates. The increase of the d_{001}-spacing
734 from left to right is closely linked to an increase of vacant sites in the octahedral sheets and
735 hydrated cations (Mg, Ni) in the interlayer spaces.

736

737 **Table 1**: Chemical analyses (wt%) of the five bulk samples.

738

Sample	Klippe	SiO_2	NiO	MgO	Fe_2O_3	Al_2O_3	LOI	Total	mole Si/∑R	mole Ni/∑R
BONBR-2c	Poro	53.6	0.0	34.5	0.71	udl	10.7	99.51	1.03	0.00
BONBR2a	Poro	49.1	26.2	15.3	0.74	udl	9.0	100.34	1.11	0.47
MG3aWill	Kon	52.8	20.3	17.7	0.12	udl	9.1	100.02	1.23	0.38
LFSTA5a2	Poro	49.0	27.6	14.3	0.71	udl	10.3	101.91	1.11	0.50
MG1aWill	Kon	47.6	37.8	5.3	0.28	udl	9.0	99.98	1.24	0.79

739 udl: under detection limit

740 Poro: sample from Poro massif (see Fig. 1)

741 Kon: sample from Koniambo massif (see Fig. 1)

742

743

744 **Table 2**: d-spacings of the major XRD peaks (Å) of the < 2 μm fractions after saturation with
745 Ca or Li in AD and EG states. For the EG state the d-spacings of the peaks at low (P1: 4-7
746 °2θ) and high (P2: 7-10 °2θ) angles are given.

747

This is a preprint, the final version is subject to change, of the American Mineralogist (MSA)
Cite as Authors (Year) Title. American Mineralogist, in press.
DOI: https://doi.org/10.2138/am-2020-6984

	MG1aWill	LFSTA5a2	MG3AWill	BON BR2a	BONBR2c
CaAD	10.04	9.95	9.92	9.92	10.20
CaEG – P1	9.95	13.10	13.80	15.12	16.47
CaEG – P2	--	9.51	9.29	9.29	8.85
LiAD	9.92	10.10	9.92	10.24	10.82
LiEG – P1	10.02	13.45	14.15	15.27	17.04
LiEG – P2	9.94	9.56	9.44	9.24	8.83

748 AD: sample analysed by XRD on air-dried state

749 EG: sample analysed by XRD after solvation with ethylene glycol

750

751 **Table 3**: Estimation of the layer charge losses of the <2 μm samples using NH_4^+ saturation
752 and measurement of the area of the infrared band at 1400 cm^{-1} before and after Li saturation
753 and heat treatment.

754

Sample	MG1aWill	LFSTA5a2	MG3aWill	BONBR2a	BONBR-2c
Klippe	Kon	Poro	Kon	Poro	Poro
Charge loss (%)	36	61	56	53	63

755

756 Poro: sample from Poro massif (see Fig. 1)

757 Kon: sample from Koniambo massif (see Fig. 1)

758

759

This is a preprint, the final version is subject to change, of the American Mineralogist (MSA)
Cite as Authors (Year) Title. American Mineralogist, in press.
DOI: https://doi.org/10.2138/am-2020-6984

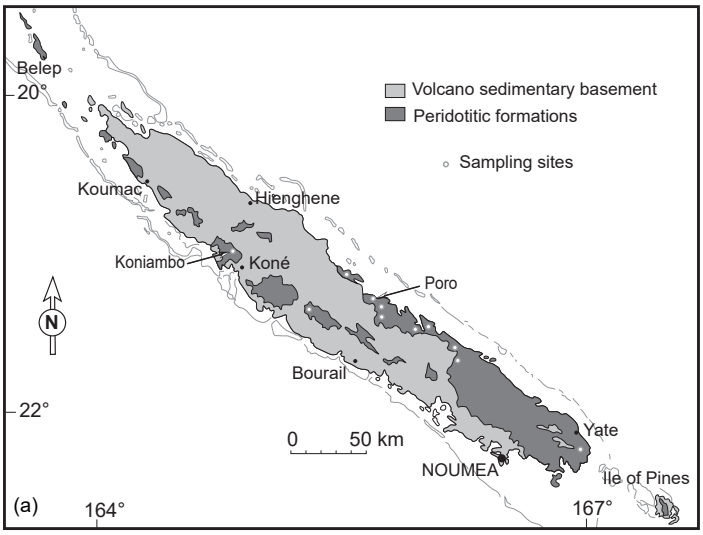

Figure 1

This is a preprint, the final version is subject to change, of the American Mineralogist (MSA)
Cite as Authors (Year) Title. American Mineralogist, in press.
DOI: https://doi.org/10.2138/am-2020-6984

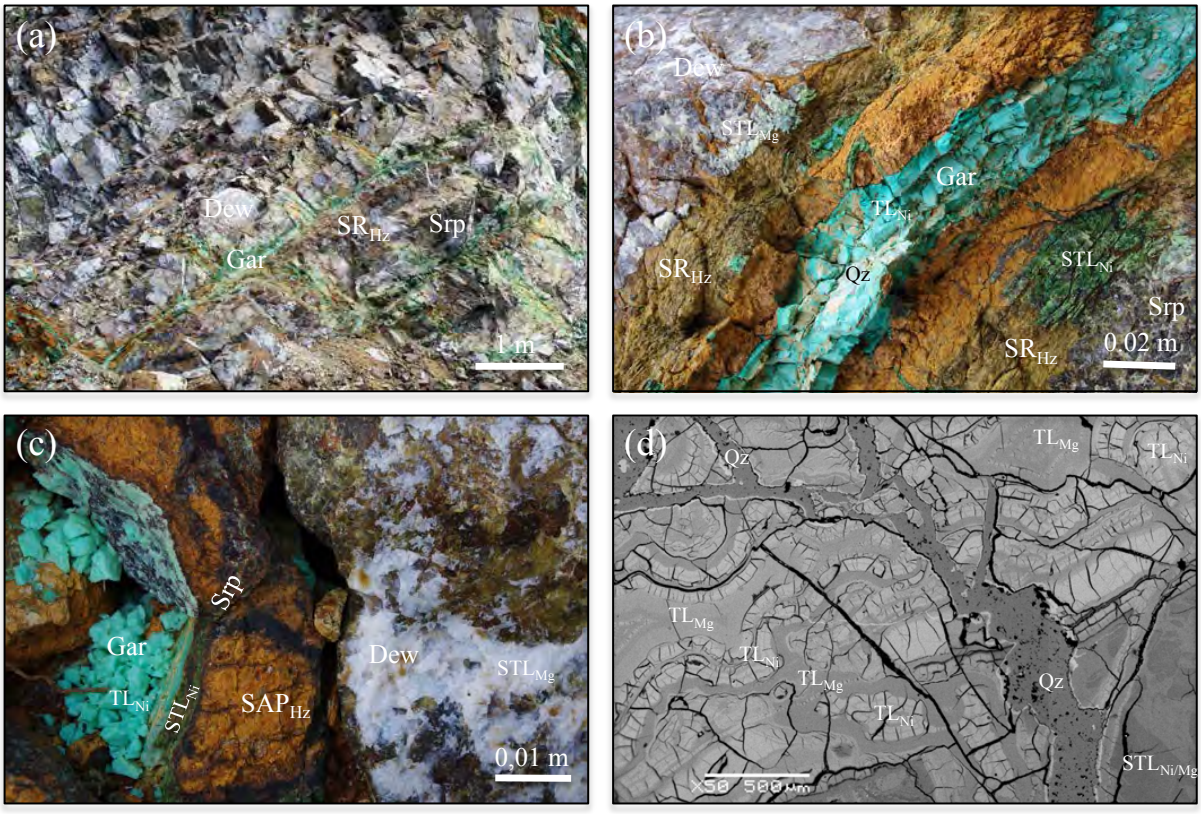

Figure 2

This is a preprint, the final version is subject to change, of the American Mineralogist (MSA)
Cite as Authors (Year) Title. American Mineralogist, in press.
DOI: https://doi.org/10.2138/am-2020-6984

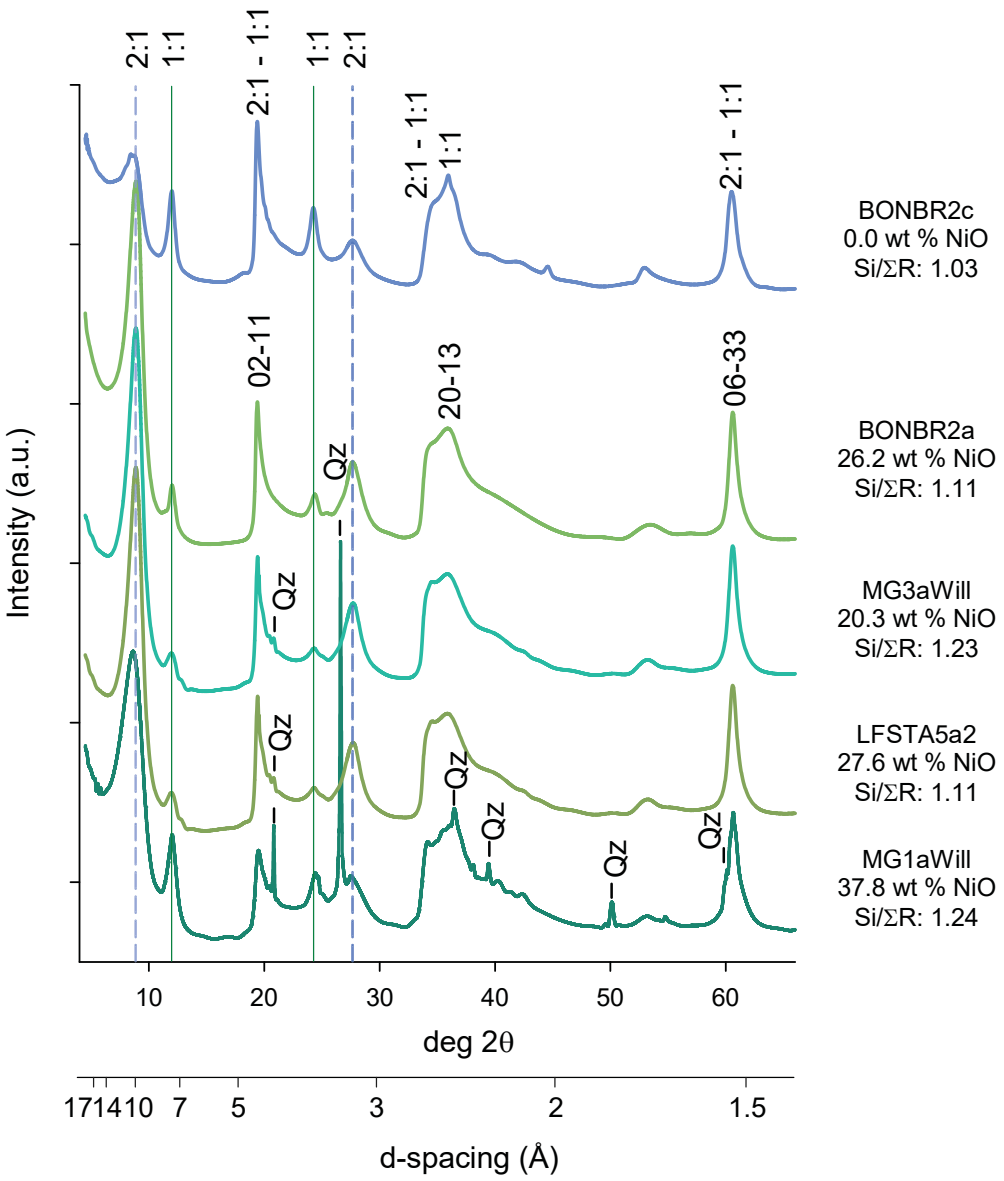

Figure 3

This is a preprint, the final version is subject to change, of the American Mineralogist (MSA)
Cite as Authors (Year) Title. American Mineralogist, in press.
DOI: https://doi.org/10.2138/am-2020-6984

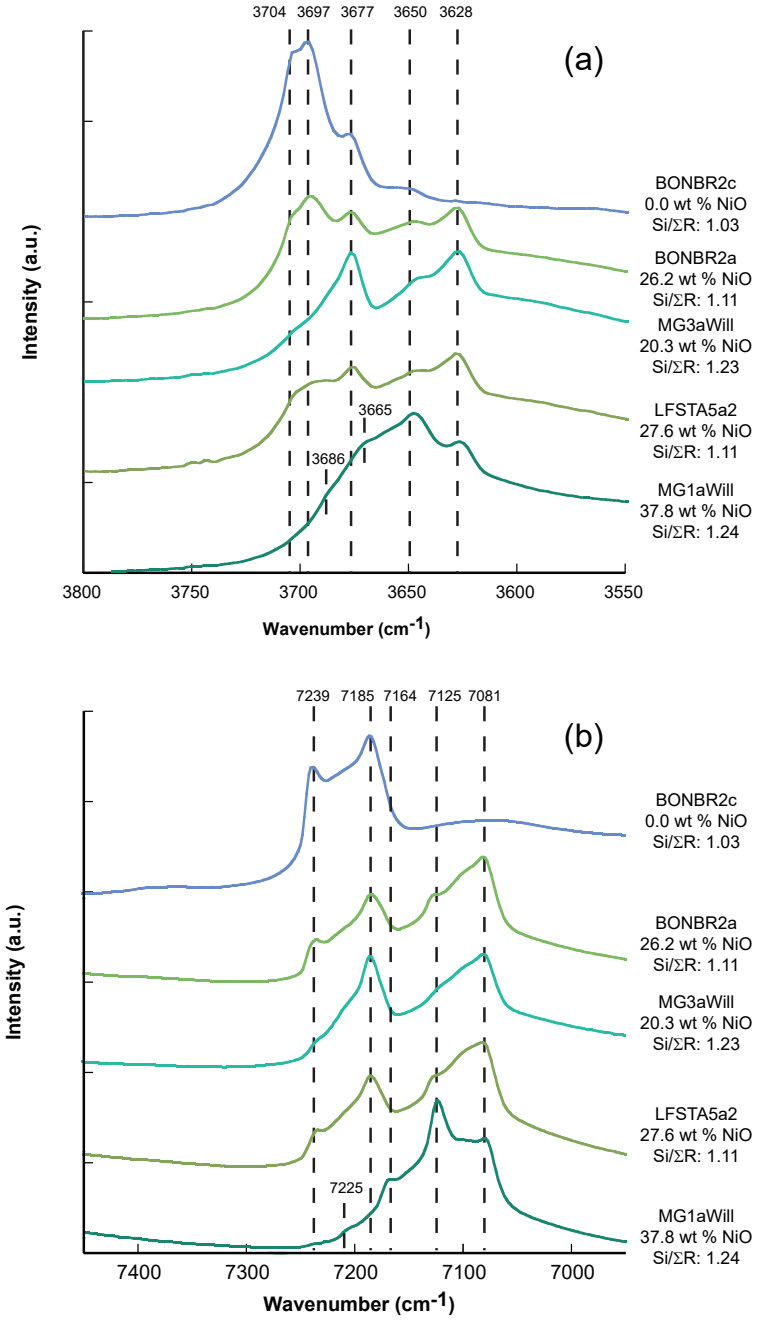

Figure 4

This is a preprint, the final version is subject to change, of the American Mineralogist (MSA)
Cite as Authors (Year) Title. American Mineralogist, in press.
DOI: https://doi.org/10.2138/am-2020-6984

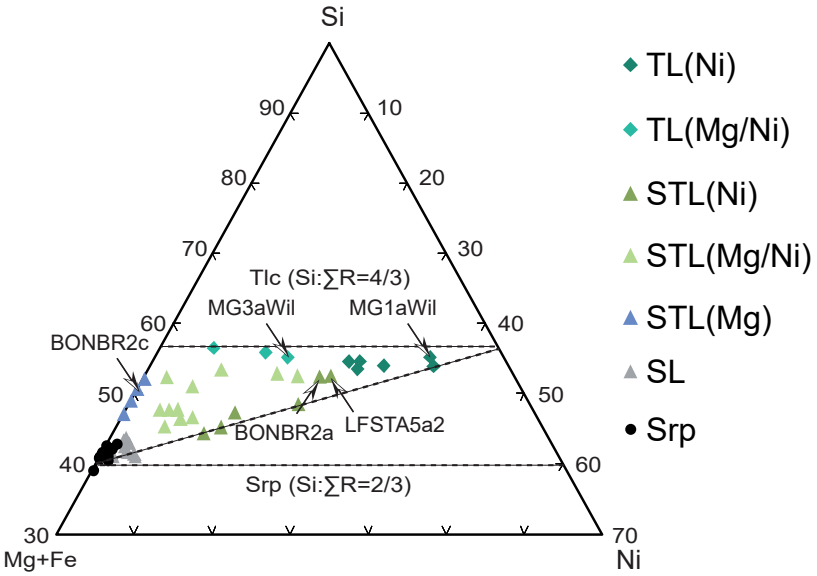

Figure 5

This is a preprint, the final version is subject to change, of the American Mineralogist (MSA)
Cite as Authors (Year) Title. American Mineralogist, in press.
DOI: https://doi.org/10.2138/am-2020-6984

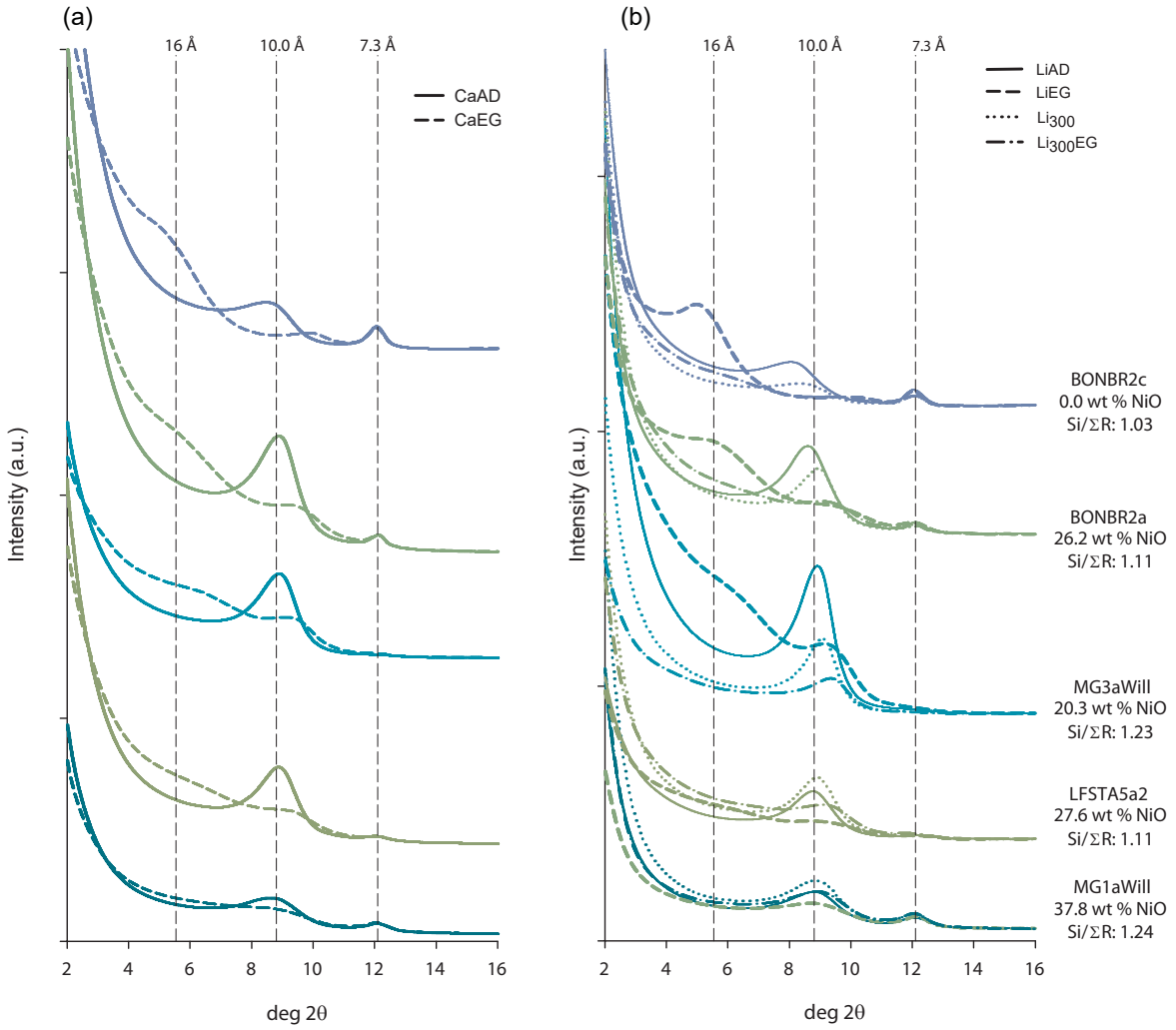

Figure 6

This is a preprint, the final version is subject to change, of the American Mineralogist (MSA)
Cite as Authors (Year) Title. American Mineralogist, in press.
DOI: https://doi.org/10.2138/am-2020-6984

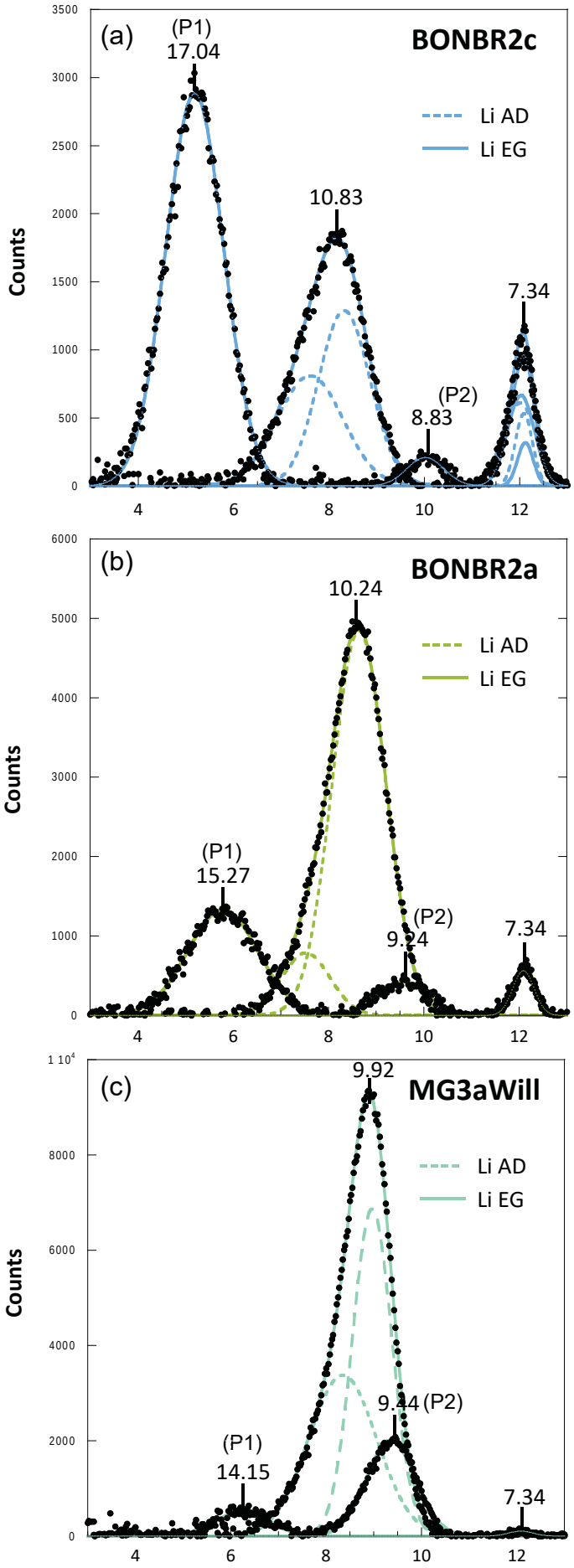

Figure 7

This is a preprint, the final version is subject to change, of the American Mineralogist (MSA)
Cite as Authors (Year) Title. American Mineralogist, in press.
DOI: https://doi.org/10.2138/am-2020-6984

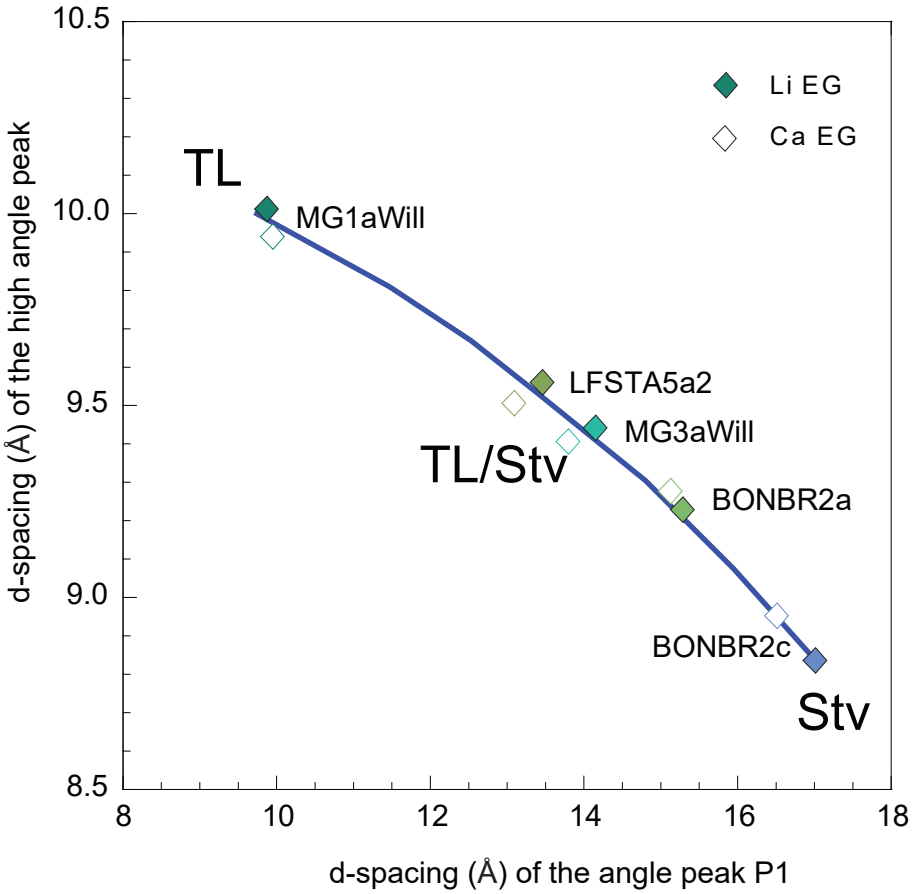

Figure 8

This is a preprint, the final version is subject to change, of the American Mineralogist (MSA)
Cite as Authors (Year) Title. American Mineralogist, in press.
DOI: https://doi.org/10.2138/am-2020-6984

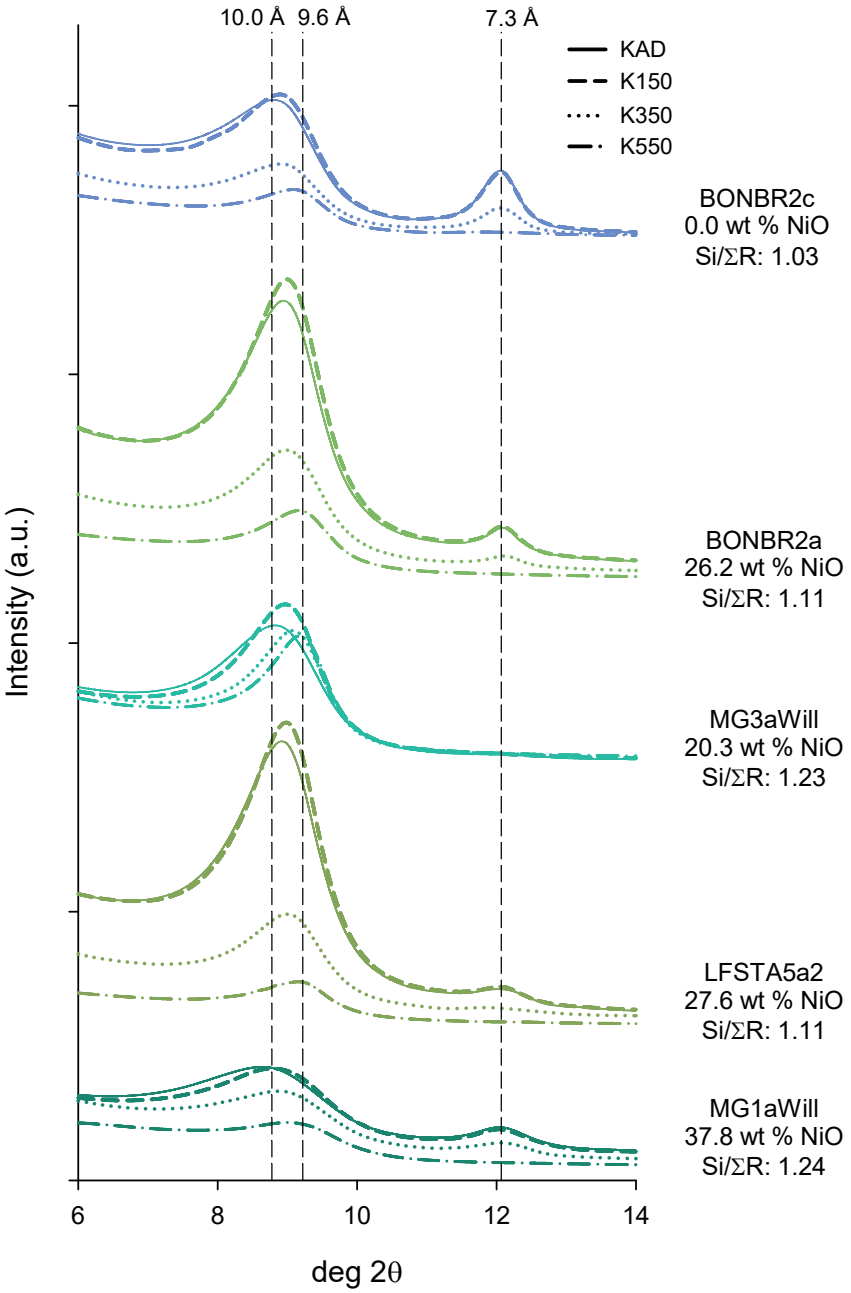

Figure 9

This is a preprint, the final version is subject to change, of the American Mineralogist (MSA)
Cite as Authors (Year) Title. American Mineralogist, in press.
DOI: https://doi.org/10.2138/am-2020-6984